J Mater Sci (2023) 58:11872–11885

Ceramics

Transparent Al_2O_3 fabricated by energy efficient spark plasma sintering

CheolWoo Park[1], Elisa Torresani[1,*], Chris Haines[2], Darold Martin[3], and Eugene A. Olevsky[1]

[1] *College of Engineering, San Diego State University, San Diego, CA, USA*
[2] *US Army DEVCOM - Army Research Laboratory, Aberdeen Proving Ground, Aberdeen, MD, USA*
[3] *US Army DEVCOM – Armaments Center, Picatinny Arsenal, Picatinny, NJ, USA*

Received: 4 April 2023
Accepted: 9 July 2023
Published online:
21 July 2023

ABSTRACT

Spark plasma sintering (SPS) techniques have been intensively investigated for manufacturing of diverse materials. Numerous sintering methods have been researched to achieve a reduction of the sintering time, larger scale production, and significant energy savings. Usually, the traditional SPS methods need prohibitively high energy outputs to fabricate transparent ceramics. Previous studies showed that the SPS input power can be significantly decreased when an energy efficient configuration using a BN-coated graphite foils is used, but many samples obtained using this approach had cracks. The developed new thermally managed SPS (TM-SPS) results in the prevention of cracks, full densification, and uniform transparency in alumina. Furthermore, consumption is 17% lower in the developed new energy efficient SPS configuration compared to the traditional SPS configuration. Therefore, the developed TM- SPS method has potential for fabricating transparent ceramic of various materials with uniform transparency. A comprehensive three-dimensional fully coupled thermo-electro-mechanical finite element framework has been used for modeling the SPS with different energy configurations.

Handling Editor: David Cann.

Address correspondence to E-mail: etorresani@sdsu.edu

Springer

https://doi.org/10.1007/s10853-023-08768-x

GRAPHICAL ABSTRACT

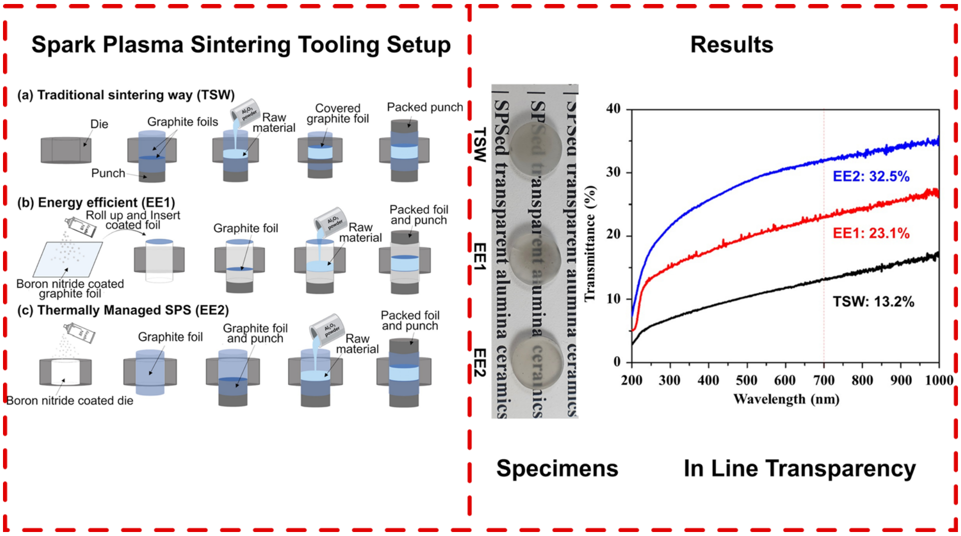

Introduction

Transparent ceramics have attracted considerable attention over the last few decades due to numerous potential applications, such as optical armor and infrared (IR) window materials, laser gain medium, and various optical elements [1–4]. Transparent ceramics have been fabricated using different sintering techniques such as hot pressing (HP), hot isostatic pressing (HIP), and pressureless sintering; however, these traditional techniques require extremely high energy for reaching high sintering temperatures and long sintering times [5–8]. For this reason, researchers have extensively focused on developing novel sintering techniques with higher energy efficiency [9, 10].

Spark plasma sintering (SPS) techniques [11] are capable of rendering a pulsed direct current passing through a green powder compact for initiating rapid sintering at high temperatures. Spark plasma occurs between powder particles, and the Joule heat is generated by the electric current passing through the powder containing graphite molds [12–14]. Consequently, this process enables the transition from low to high temperatures (> 2000 °C) within a shorter time compared to more traditional sintering techniques due to the thermal factors and electric field effects [15, 16].

Regarding the advantages of the energy efficiency of this technology, the first is the reduction of the sintering time. Universally, previous studies indicated that fabrication of high-density ceramics requires reactive sintering aids to enhance the diffusion coefficients and mass transfer for fast densification [17–19]. Recently, the development of flash sintering (FS) showed that a transition at high temperature from electrically insulating to electrically conductive behavior has allowed the sintering of ceramics in a few seconds (3–5 s) under low power dissipation conditions [20–22].

The second advantage of the energy efficient SPS is the scaling up capabilities. To overcome the problem of limited volume dimensions, consolidation of large size specimens of SiC (60 mm in diameter) can be completed within minutes using the flash spark plasma sintering (FSPS) [23]. Similarly, Dimirskyi et al. demonstrated using a mold-free SPS setup approach to produce dense SiC ceramics with a diameter of 30 or 50 mm [24]. However, in both cases, a high electric power supply is needed. Concerning the fabrication of large components, the more efficient high energy delivery by the power supply is the key consideration.

The third advantage of the energy efficient SPS is energy saving. The commercial SPS systems' upper current limit is around 20–30 kA allowing to sinter samples of about 35–40 cm diameter [25]. This size limitation is rather limited, considering the amount of electric current involved. Therefore, to prevent the problem of wasteful energy consumption, the overall SPS process should be engineered to make more efficient use of the high energy delivered by the power supply. Optimization of the SPS tooling design to deal with excessive heating phenomena has enabled the avoidance of the wasted overheating energy [26]. In a previous study [27], we showed that the net shape FSPS method, in which the sample exhibited a stable and ultra-rapid densification with homogeneous microstructures, can be rendered by concentrating the electric current and confinement of the heat generated. Also, using an energy efficient method where the electric current was lower than 1000 A was constrained in the graphite foil around the sample, it was possible to fully sinter up to 40 mm diameter alumina samples [28].

In this study, three types of SPS tooling configurations called "traditional sintering way (TSW)" and "energy efficient 1 (EE1)" and "thermally managed SPS (TM-SPS or EE2)" have been considered, where EE1 and EE2 produced alumina transparent ceramics using boron nitride spray (Fig. 1). All specimens are compared and analyzed to check sample properties and energy savings. In addition to experimental verification, the feasibility of this method is tested by the electric-thermal–mechanical finite element SPS process simulation.

Material and methods

Consolidation by three different methods

An alumina powder Al_2O_3 (Sumitomo Chemical, AA-3, single crystals with mean particle size 3.5 µm) was used as the starting material. To perform the TSW experiment, 1.5 g of Al_2O_3 powder was poured into a 15 mm diameter graphite die, wrapped with graphite foils, and packed by the punch. In the EE1 configurations, the external graphite foil was coated using a boron nitride spray and inserted inside the die after drying for 30 min. Then 1.5 g of Al_2O_3

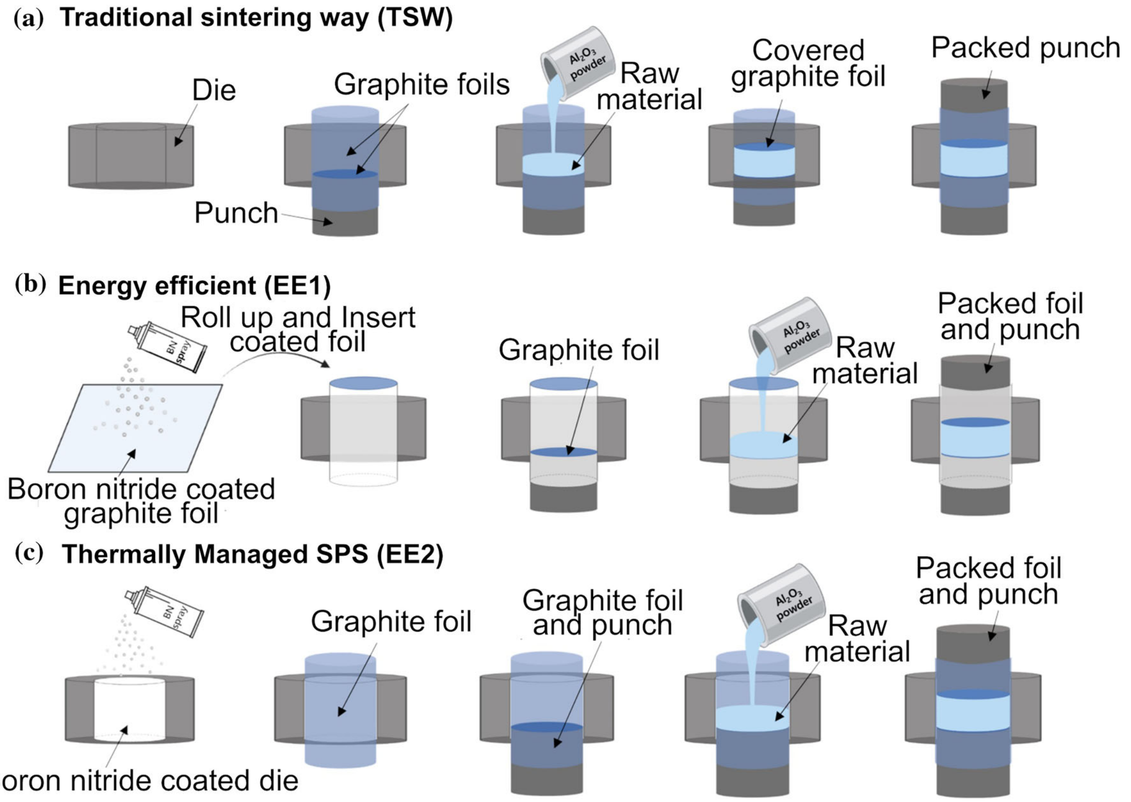

Figure 1 SPS tooling configurations: **a** TSW, **b** EE1, and **c** EE2.

powder was poured into the die and packed by the punch. In the EE2 configurations, the inside walls of the die were coated by boron nitride spray and dried for 30 min, and 1.5 g of Al_2O_3 powder was poured into a 15 mm diameter graphite die wrapped with graphite foils and packed by the punch. Thereafter, these dies were sintered using a spark plasma sintering system (SSPS DR. SINTER Fuji Electronics model 515, Japan). The sintering conditions were as follows: (i) the entire process was conducted at 10 Pa vacuum and pressure of 70 MPa; (ii) the die was heated at 100 °C/min from room temperature to the final sintering temperature (1300 °C) for 50 min; (iii) after sintering, the pressure was released, and the electric current was cut off.

Sample processing and characterization

The measurement of temperature was conducted by a radiation thermometer (temperature range: 570–3000 °C), which was focused on the surface of the graphite die. The temperature, pressure, current, voltage, and vacuum conditions were recorded every 1 s. And for every selected processing profile, an additional SPS run was conducted in the absence of powder, and the axial displacement obtained from this idle run was subtracted from the displacement retrieved to calculate the actual axial shrinkage of a specimen.

The final bulk density of the specimens was measured using the Archimedes' method following ASTM standard C373-18; moreover, the final dimensions were measured using a caliper.

In the sintered specimen, the surfaces of both sides were polished with a 3 μm diamond slurry. In-line transmittance and absorption were measured in a wavelength range of 300–1000 nm using a UV–Vis-NIR spectrophotometer (Cary 50, UV–Vis Spectrophotometers, Varian, UK). Afterward, all samples have been polished and thermally etched in an electric furnace at 1100 °C for 30 min in order to analyze the average grain size by field-emission scanning electron microscopy (SEM, Quanta-450, FEI, Czech Republic) at acceleration voltages of 5–15 kV. The Vickers hardness of the sintered bodies was determined after polishing using a digital macro-Vickers hardness tester (900–398, Phase II, USA). A square-based pyramidal diamond indenter was used by applying a load of 1 kg for 15 s. Each group consisted of three samples was measured 20 times and these measurements were averaged.

SPS Modelling

The coupling of electrical, thermal, mechanical (stress–strain), densification, and grain growth components involved during the three SPS process' configurations is carried out using a macro-scale model incorporated in COMSOL™ finite element software. The model's framework and boundary conditions are described below.

Models for considered physical phenomena

The model couples the following five components: (a) electrical current's flow, (b) Joule heating, (c) mechanical deformation, (d) densification, and (e) grain growth. The first two involve the graphite tooling and the graphite foil, considering the different conductivity at their interface induced by the presence of the boron nitride layer. The last three components are considered for the powder compact.

(a) *Electrical Current Flow:* The conservation of electrical current is expressed as:

(b) $\nabla \cdot \vec{J} = 0$ where the current density $\vec{J}$ is related to the electric field $\vec{E}$ though the electrical conductivity λ: $\vec{J} = \lambda \vec{E}$.

Considering a static problem where $\nabla \times \vec{E} = 0$ the electric field can be defined in terms of electrostatic potential V: $\vec{E} = -\nabla V$. The combination of these relationships results in a second-order partial differential equation:

$$\nabla \cdot \vec{J} = \nabla \cdot \left(\lambda \vec{E}\right) = \nabla \cdot |\lambda(-\nabla V)| = -\nabla \cdot (\lambda \nabla V) = 0 \tag{1}$$

(c) *Joule Heating and Heat Transfer:* The energy conservation defined as:

$$\rho C_p \frac{\partial T}{\partial t} + \nabla \cdot \vec{q} = h \tag{2}$$

presents the time dependence of the temperature in terms of heat flux $\vec{q}$ and heat generated h by the electric current density in the material. In Eq. 2, the other parameters present are the density (ρ) and the heat capacity (C_p). The heat flux vector is defined as $\vec{q} = -k_T \nabla T$, where k_T is the thermal conductivity of the material and the heat generated as $h = \vec{J} \cdot \vec{E}$. Considering all these relationships results in a second-order partial differential equation:

$$\begin{aligned} \rho C_p \frac{\partial T}{\partial t} + \nabla \cdot \vec{q} &= \rho C_p \frac{\partial T}{\partial t} + \nabla \cdot (-k_T \nabla T) \\ &= \rho C_p \frac{\partial T}{\partial t} - \nabla \cdot (k_T \nabla T) = \left|\vec{J}\right| \left|\vec{E}\right| \end{aligned} \tag{3}$$

The induced Joule heating can be described coupling the relationship for the conductive media DC expressed by Eq. 1 and the heat transfer by conduction (Eq. 2):

$$\begin{cases} \nabla \cdot (\lambda \nabla V) = 0 \\ \rho C_p \frac{\partial T}{\partial t} - \nabla \cdot (k_T \nabla T) = \lambda |\nabla V|^2 \end{cases} \tag{4}$$

(d) *Densification (Sintering Model):* The main constitutive equation for the sintering of a nonlinear viscous porous material can be defined as [29]:

$$\sigma_{ij} = \frac{\sigma(W)}{W} \left[\varphi \dot{\varepsilon}_{ij} + \left(\psi - \frac{1}{3} \varphi \right) \dot{e} \delta_{ij} \right] + P_L \delta_{ij} \tag{5}$$

where σ_{ij} represent the externally applied stresses, $\sigma(W)$ is the effective stress, W *is* the equivalent strain rate, $\dot{e}$ is the shrinkage rate, $\dot{\varepsilon}_{ij}$ is the strain rate components, and δ_{ij} is the Kronecker's delta. The normalized shear and bulk viscosity modulus φ and ψ, respectively, and the effective sintering stress P_L can be written as a function of porosity θ:

$$\varphi = (1 - \theta)^2 \tag{6}$$

$$\psi = \frac{2}{3} \frac{(1 - \theta)^3}{\theta} \tag{7}$$

$$P_L = \frac{3\alpha}{r_0} (1 - \theta)^2 \tag{8}$$

where α [J m^{-2}] is the surface energy of the material, and r_o [m] is the average particles size.

The effective stress and the equivalent strain rate for the case of power law creep case can be defined as:

$$\sigma(W) = A W^m \tag{9}$$

$$W = \frac{1}{\sqrt{1 - \theta}} \sqrt{\varphi \dot{\gamma}^2 + \psi \dot{e}^2} \tag{10}$$

where A and m are material constants and $\dot{\gamma}$ corresponds to the shape change rate. In a three-dimensional Cartesian coordinate system (x, y, z), the shrinkage and shape rate change can correspond to:

$$\dot{e} = \dot{\varepsilon}_x + \dot{\varepsilon}_y + \dot{\varepsilon}_z \tag{11}$$

$$\dot{\gamma} = \sqrt{2\left(\dot{\varepsilon}_{xy}^2 + \dot{\varepsilon}_{xz}^2 + \dot{\varepsilon}_{yz}^2\right) + \frac{2}{3}\left(\dot{\varepsilon}_x^2 + \dot{\varepsilon}_y^2 + \dot{\varepsilon}_z^2\right) - \frac{2}{3}\left(\dot{\varepsilon}_x \dot{\varepsilon}_y + \dot{\varepsilon}_x \dot{\varepsilon}_z + \dot{\varepsilon}_y \dot{\varepsilon}_z\right)} \tag{12}$$

The temperature dependence of the pre-exponential factor in Eq. (9) can be defined through an Arrhenius equation:

$$A = A_0 T^m \exp\left(\frac{mQ}{\mathrm{RT}}\right) \tag{13}$$

where A_0 is a power law creep factor, T is the absolute temperature, R is the gas constant, and Q is the power law creep activation energy.

The porosity θ determines the general behavior of the porous material. The density of the material (ρ) and the porosity can be related through the relationship:

$$\rho = \rho_{Th} (1 - \theta) \tag{14}$$

where ρ_{Th} is the theoretical density of the fully densified material. The densification of the material can be determined though the porosity's evolution, which can be defined using the continuity equation:

$$\frac{\dot{\theta}}{1 - \theta} = \dot{e} \tag{15}$$

(e) *Grain Growth*: The temperature dependence of the grains' size can be defined as [30]:

$$\frac{\mathrm{dG}}{\mathrm{dt}} = \frac{k_0}{3G^2} \left(\frac{\theta_c}{\theta + \theta_c} \right)^{\frac{3}{2}} \exp\left(-\frac{Q_G}{\mathrm{RT}} \right) \tag{16}$$

where the materials parameters k_0 [m^{3}s^{-1}] and Q_G [kJ K^{-1} mol^{-1}] are, respectively, the pre-exponential factor and the activation energy for the grain growth, and θ_c is a critical value which represents the transition from open to closed porosity. The grain growth influence on the behavior of the porous material can be included in Eqs. (8) and (13) and modifies them as follows:

$$P_L = \frac{3\alpha}{G}(1-\theta)^2 \tag{17}$$

$$A = A_0 T^m \exp\left(\frac{mQ}{\mathrm{RT}}\right)\left(\frac{G}{G_0}\right)^2 \tag{18}$$

where G_0 [μm] is the initial average grain size.

The material parameters used in the model are present in Table 1.

Coupling of the multi-physics components

The electrical properties are defined as functions of temperature to couple the thermal and electrical problems. Furthermore, the heat capacity and thermal conductivities are defined as temperature's functions. Similarly, electrical and thermal transfer properties are expressed as a function of porosity. The mechanical, thermal, porosity and grain growth components are coupled through the equations which define the power law creep (PLC) Eqs. (9), (10), and (18), sintering stress (17), and the grain growth model (16).

The system of partial differential equations described above is embedded in the finite element software COMSOL$^{\mathrm{TM}}$ which allows assigning simultaneously all the boundary conditions (thermal, electrical and mechanical) enabling a multiple way coupling of multi-physics phenomena.

To consider the difference between the three configurations the electrical contact condition between the die, the punches were changed to consider the presence of the boron nitride layer.

Results and discussions

Output power validation and densification behavior

Recorded data obtained by TSW, EE1 and EE2 were investigated with regard to the consolidation efficiency of Al_2O_3 during SPS processes (Fig. 2a, b and c). The SPS experiments were conducted under the same sintering conditions while maintaining the same pressure (70 MPa) from the beginning to the end of the SPS. The differences in the electric current value for TSW, EE1 and EE2 (TM-SPS) are obviously related to the sintering temperature. All electric current values are slightly reduced and plateaued, but the differences remain constant after 1300 °C. Then, for all SPS tooling configurations, powder specimens were densified for 45 min at different electric current outputs. The EE1 and EE2 configurations show a very high efficiency of the heating with electric current values of about 310 A and 450 A, respectively, up to 1300 °C; these configurations render lower efficiencies of about 43% and about 17%, respectively, than TSW. The TSW configuration has profusely generated high amount of electric current passing through Al_2O_3 at a high temperature during the SPS process.

Table 1 Parameters Eqs. 16, 17 and 18

k_0 [$m^3 s^{-1}$]	3.0 10^{-4}
θ_c [-]	0.08
Q_G [J K^{-1} mol^{-1}]	490,000
α [J m^{-2}] [30]	1.12
A_0 [Pa s]	2.35 10^{-3}
m [-]	1
Q [J K^{-1} mol^{-1}]	144,000
G_0 [μm]	3.5

From the obtained densification curves for TSW, EE1 and EE2 configurations the densification behaviors have been calculated and plotted as shown in Fig. 2d, e and f. The final density reached about 99% for TSW, about 98% for EE1, and about 99% for EE2, respectively. From the measurements of the specimens' final dimensions, a consistent diameter of 15 mm for all the produced specimens has been determined.

In contrast to the TSW behavior, the EE1 and EE2 densification behaviors tended to accelerate densification rate from 600 °C to 1300 °C. The configuration of EE2 showed interesting results, achieving density of about 83.6% at the end of the ramp up period. This indicates that the energy efficient SPS methods are more sensitive to the accelerated sintering kinetics, apparently due to the heat generated from the die inducing conduction into the inside of the specimen due to the insulation of boron nitride [26, 28].

Transmittance of alumina samples fabricated by different tooling setups

Figures 3 and 4 show, respectively, the images and measurements of the in-line transmittance (2.0 mm in

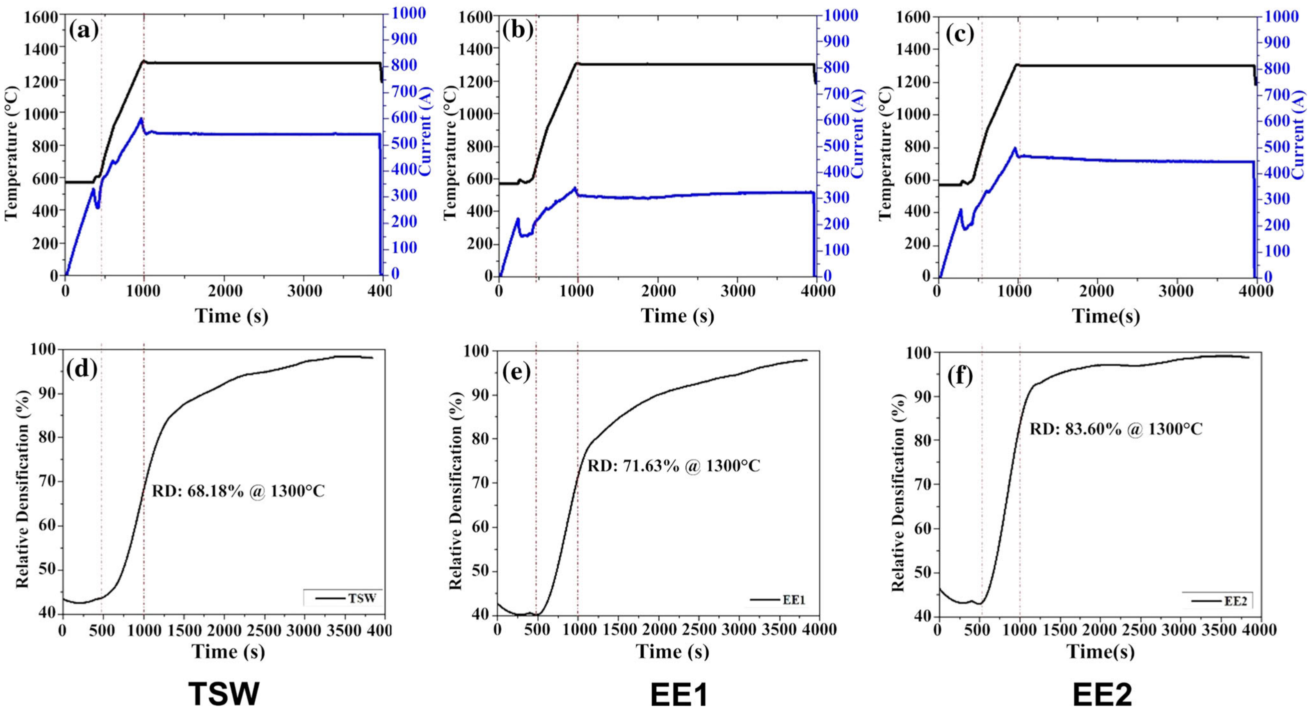

Figure 2 Experimental analysis of the TSW, EE1 and EE2 (TM-SPS) configurations; the temperature, electric current and samples relative density.

Figure 3 Photographs of transparent Al_2O_3 ceramics (2.0 mm in thickness) fabricated by different tooling setups.

thickness) of all the polished specimens sintered by different tooling setups. Specimens manufactured in all configurations are transparent enough to clearly view text directly behind samples.

However, in the alumina transparent ceramic fabricated by the TSW and EE1 configurations, a dark area exists in the center of the specimen. This implies that the SPS tooling configurations render different outcomes. In the case of TSW, the fabricated specimen has a higher transparency only near the edge through generating a different sintering temperature gradient between the specimen's edge and center during the SPS process.

On the other hand, EE1 and EE2 configurations render specimens with higher transparency, and in the case of the TM-SPS configuration even in the vicinity of the center which results in a uniform specimen. This stems from the temperature uniformity provided by a thermal confinement effect due to the high resistance-generated heat shown in Fig. 4. (The in-line transmittance of all samples showed TSW about 13.2%, EE1 about 23.1%, and EE2 about 32.5% at 700 nm wavelengths at the center, respectively.) But the specimens fabricated in EE1 configuration exhibited several cracks at the edge of the sample. It is possible that the EE1 configuration is more sensitive to the properties of the electric contacts, so that it can generate a thermal shock during the SPS process. Contrastively, the EE2 configuration rendered no cracks due to a more uniform

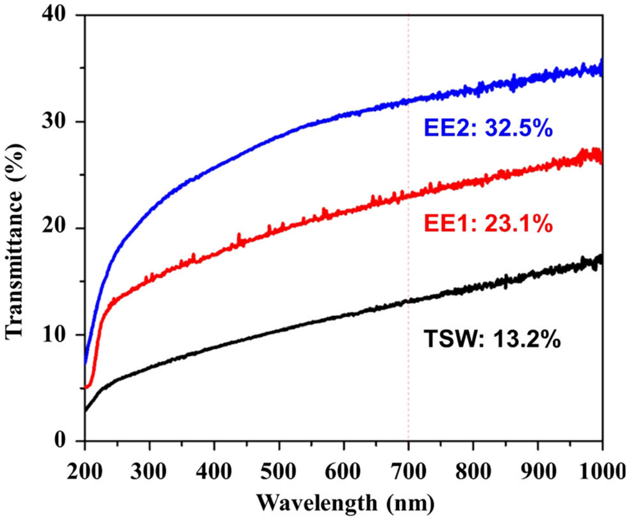

Figure 4 Transmittance of transparent Al_2O_3 ceramics (2.0 mm in thickness) by different configurations.

temperature gradient than in the other methods; despite its high ramp rate (100 °C/min) the densification progressed in a thermodynamically stable manner. Therefore, EE2 (TM-SPS) provides an efficient regime to obtain high transparent alumina ceramic samples in spite of low power consumption (see discussion on the comparison of the experimental and modeling results in in Sect. "Comparison of modeling and experimental results").

Microstructure evolution rendered by different SPS tooling configurations

The variations in transparency can be explained by a descriptive analysis of the microstructure evolution for different SPS tooling configurations (Fig. 5). Three different regions of each sample were inspected, in the cross-sectional area, including center and edges after thermal etching process in order to see the effect of the different SPS tooling setups.

The average grain size, porosity, pore size, and morphology varied significantly for different SPS tooling configurations. It is well-established that to attain high transparency in alumina ceramics, reducing the sources of light scattering and absorption, such as grain boundaries and pores, are the key factors [29]. The fabricated samples have shown a dense, uniform microstructure, with no abnormal grain growth observed; however, some micro-pores are observed at grain boundaries. In general, sintering in a vacuum or hydrogen atmosphere will result in black discoloration in oxide ceramics, which have been extensively reported. The oxygen vacancies and

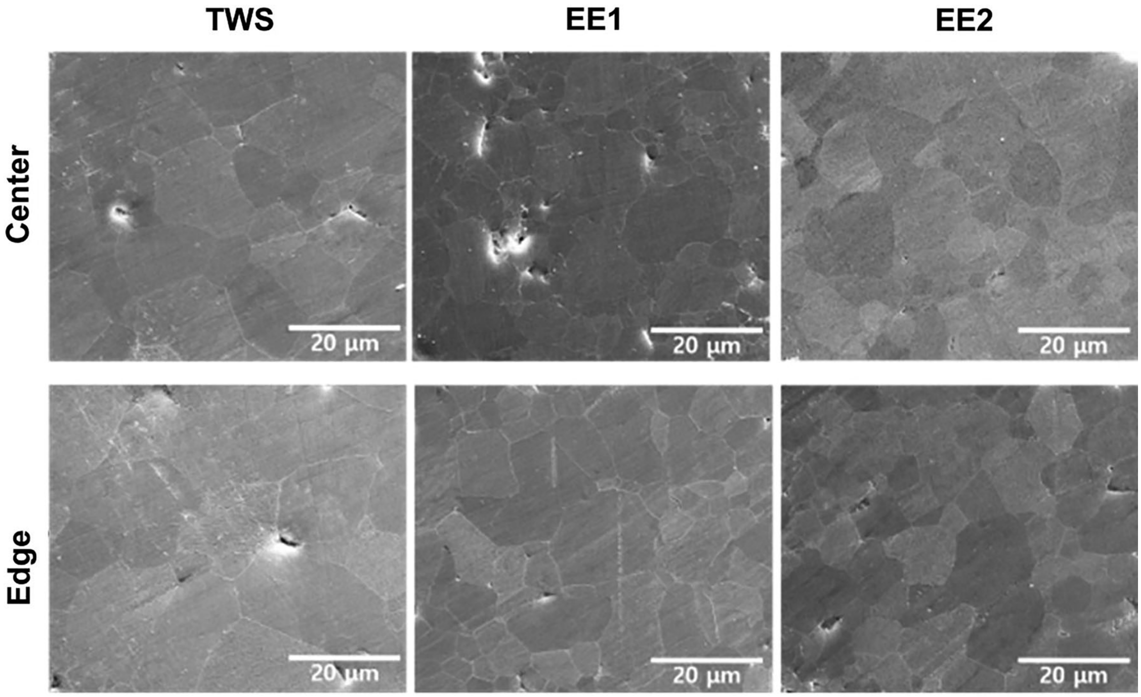

Figure 5 SEM images of microstructure at the edge and center regions of thermal etched surface for the TSW, EE1 and EE2 configurations.

color centers are the main sources of the discoloration, along with potential carbon contamination from the graphite/graphite foil in the TSW tooling configuration during the high temperature sintering process [30]. In the sample sintered with the TSW configuration, the average grain size was nearly the same at the center as in the edge regions, and pores were significantly larger than for other SPS tooling configurations. In the EE1 configuration, a few relatively large grains and elongated pores are present in the specimen's center, so that this sample obtained lower relative density than the others while having small pores formed at the edge [32]. Interestingly, in the EE2 configuration, there was less residual porosity and smaller size of micro-pores. Consequentially, in the EE1 experiment, it was a very important achievement that the entire sample became transparent without other process such as annealing to remove voids and the black color in the center.

Moreover, the grain growth rate showed noticeable reduction from the traditional SPS tooling method (Fig. 6). Despite the identical powder and sintering temperature, the grain and the pore size are quite different depending on the SPS tooling configurations. In the EE1 and EE2 configurations, it can be seen that the grain size is smaller than when the conventional SPS tooling is used. In terms of the average grain size, the TSW specimen had grains of relatively large size (13.03 μm), followed by the EE2 configuration (6.64 μm) and the EE1 configuration (5.74 μm). The grain size of the alumina in TSW tooling is about twice as large as that of the BN-coated tooling configurations (EE1 and EE2 samples). The smaller grain size makes the higher transmittance in the presence of some residual pores [33].

In the TSW configuration, only the vicinity of the center is intensively heated through the interface between punch and alumina powder; therefore, the average grain size in the center is relatively large compared to the edge [25]. In the EE1 configuration, it was observed that the average grain size at near the edge is much larger because the temperature near the edge is higher than in the center due to the insulation by BN. Interestingly, it was observed in the EE2 configuration that the average grain size of the center is relatively large compared to the edge, even though this configuration also uses BN to insulate the inside of the die. Comparing the configuration of energy efficient methods EE1 and EE2, the average grain size of the EE1 specimen was less uniform compared to that of the EE2 specimen, and the presence of many micro-pores was observed. This can lead to light scattering and absorption; therefore, transmittance decreases in the EE1 specimens. Thereby reducing the residual porosity has more of an effect on transparency than reducing the grain size [34]. The cause of the low transmittance and light scattering of specimens may be related to the presence of residual pores [35].

Vickers hardness measurements

Figure 7 presents the Vickers hardness of the Al_2O_3 transparent ceramics for different SPS tooling configurations. Each data point is an average of 20 indents and all the indents were created by applying a 1 kg load. Overall, the hardness values of the samples showed a small increase with decreasing grain size (TSW:1714.5 HV, EE1:1795.4 HV, and EE2: 1800 HV). Because of the presence of more grain boundaries in the samples with smaller grain size, restricting the free path of dislocations results in the

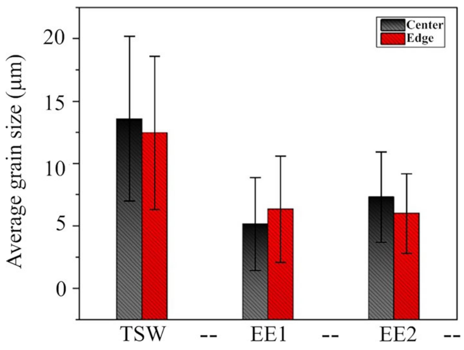

Figure 6 Average grain size at the center and edge regions for different SPS tooling configurations.

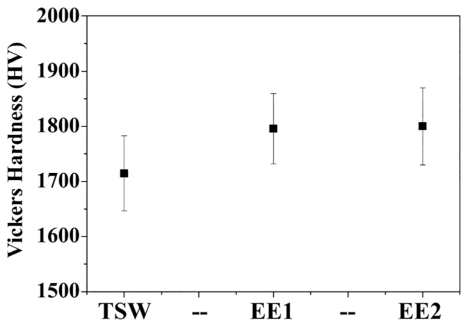

Figure 7 Vickers hardness of Al_2O_3 transparent ceramics by the TSW, EE1 and EE2 configurations.

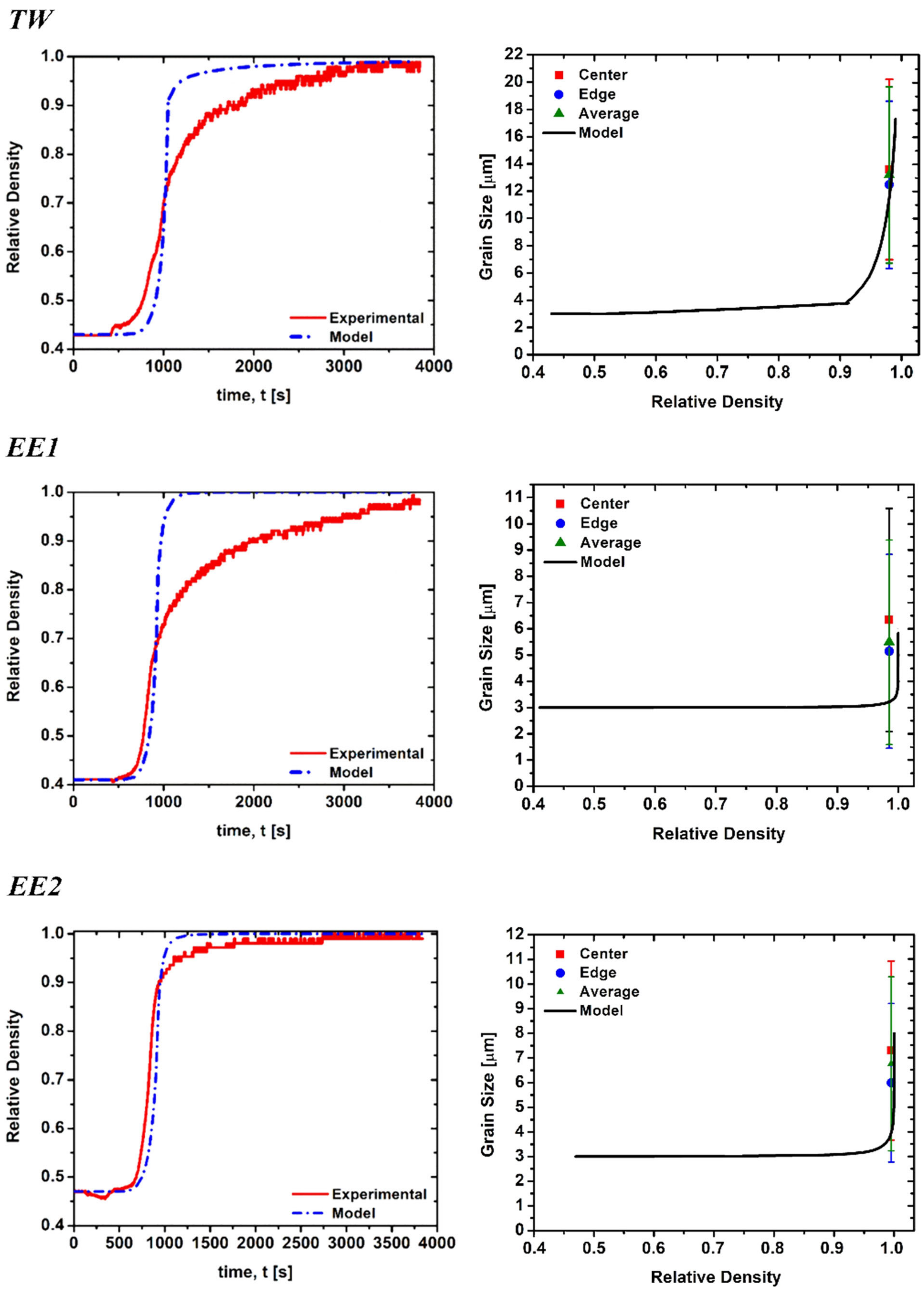
TW
Relative Density
time, t [s]
Experimental
Model
0.4
0.5
0.6
0.7
0.8
0.9
1.0
0
1000
2000
3000
4000
Grain Size [μm]
Relative Density
Center
Edge
Average
Model
0
2
4
6
8
10
12
14
16
18
20
22
EE1
Relative Density
time, t [s]
Experimental
Model
Grain Size [μm]
Relative Density
Center
Edge
Average
Model
0
1
2
3
4
5
6
7
8
9
10
11
EE2
Relative Density
time, t [s]
Experimental
Model
0
500
1000
1500
2000
2500
3000
3500
4000
Grain Size [μm]
Relative Density
Center
Edge
Average
Model
0
1
2
3
4
5
6
7
8
9
10
11
12

◀**Figure 8** Comparison between experimental data and model results for densification and grain growth for the TSW, EE1 and EE2 configurations.

reduction in plastic deformation [36, 37]. Besides, the reduction of the pore contents in ceramics could certainly improve mechanical properties and resist the deformation effectively. Therefore, the sample obtained by TSW has a large number of pores and grain size should be the dominant factor, therefore the hardness value was apparently lower for the TSW specimens than that of the EE2 specimens.

Comparison of modeling and experimental results

The simulation obtained using the model described in Sect. ″SPS Modelling″ provided the results for the three SPS tooling configurations (TW, EE1 and EE2). In Fig. 8, the comparison between experimental data and model results for the densification and grain growth shows a satisfactory agreement.

Figure 9 displays the outputs of the finite element modeling code in terms of the relative density and grain size distribution in the sintered specimens and electric current density in the tooling during the sintering process for the three different conditions.

As can be noticed from the experimental and modeling results (Figs. 2 and 8), the main difference between the three SPS setup configurations is the electric contact present between the punches/specimen and the die. The presence of the boron nitride coating inhibits and/or reduces the electric conductivity between these elements. The electric current is forced to mainly pass through the graphite paper resulting in a localized increase in the electric current density (Fig. 8). Consequently, avoiding dispersion of the electric current in the external die results in a more efficient Joule heating close to the specimen. This new electric current pattern, which localizes heat generation, results in a more uniform heating, as can be noticed from the final microstructure. In the traditional setup, where the electric current is free to flow in the die, it can be noticed how the grain size is the greatest, with pores mainly localized in the center of the specimens resulting in lower transparency. For EE1 and EE2 configurations, the final grain size was smaller and generally more uniform, which resulted in the improved transparency of these specimens. However, EE1 also shows non-uniform transparency due to the presence of defects in the center, as indicated in Fig. 4. Moreover, the specimens produced

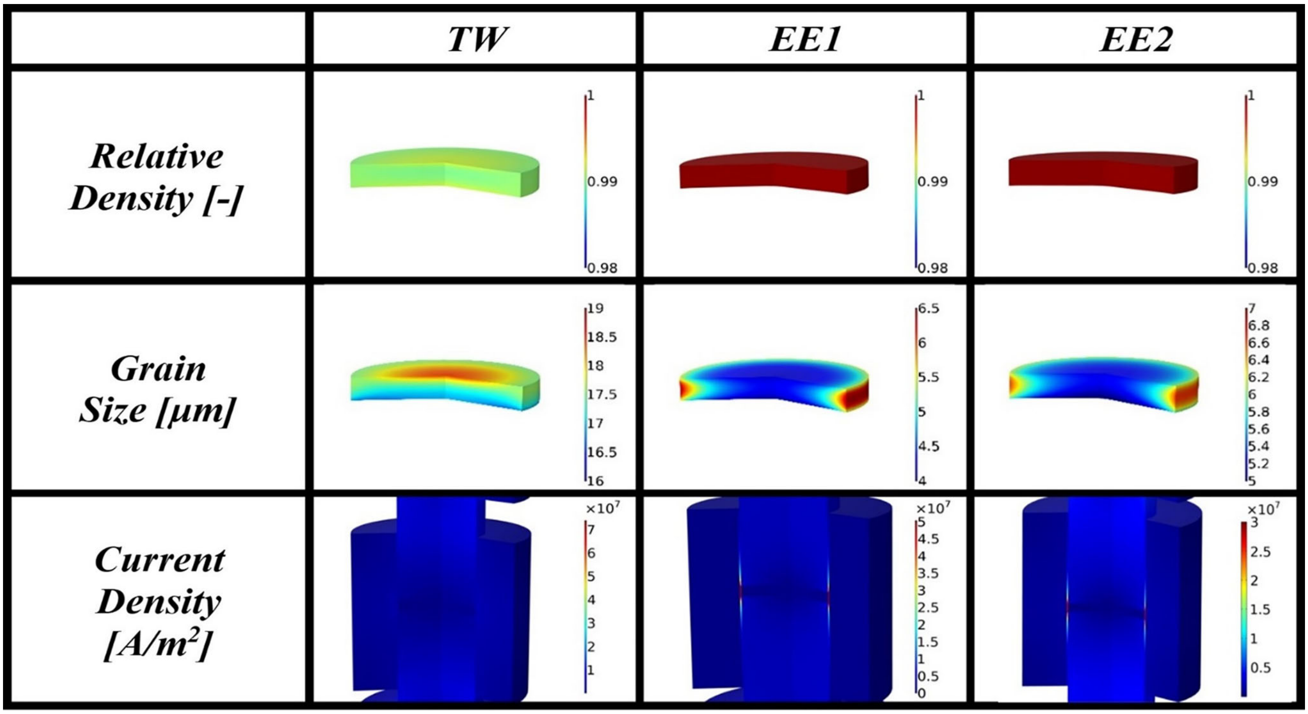

Figure 9 FEM model results for the TSW, EE1 and EE2 configurations.

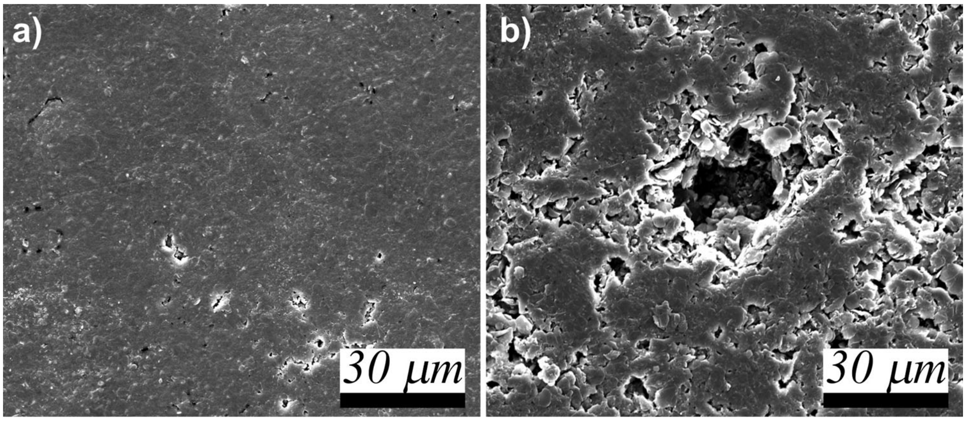

Figure 10 Boron Nitride coating applied on **a** graphite paper, **b** graphite tooling.

with this method show cracks localized at the lateral surface. This edge cracking can be associated with the sample reaching the critical thermal shock temperature due to the highly localized heating near the die wall. In the EE2 (TM-SPS) setup, this phenomenon is not present since the boron nitride applied directly to the internal cavity has lower electrical resistance, allowing it to avoid the thermal shock temperature and maintain a small and uniform grain size in the specimen. The lower value of the electric resistivity in EE2, in comparison with EE1, can be explained by the structure morphology of SPS graphite tooling, which presents small, uniformly distributed porosity, that can reduce the structure non-uniformity due to the applied boron nitride layer (Fig. 10).

The BN applied to the graphite paper (Fig. 10a) appears uniform and compact with few small defects. On the contrary, the coating applied to the graphite tooling appears to be less homogeneous and not defect-free. The presence of defects in the BN coating applied on the surface of the die cavity (Fig. 10b) in EE2 configuration allows a small quantity of electrical current to pass into the die and therefore avoid reaching the thermal shock temperatures close to the specimen's surface.

Therefore, the model and its results indicate a more uniform localization of the heating and the temperature generated in the thermally managed SPS (EE2 configuration) to obtain uniform transparent ceramics. This capability will be even more important with the increasing of the specimens' size to allow a thermo-electric contact enabling the improvement of the homogeneous temperature distribution and the decrease in the energy consumption by the sintering process.

The proposed model is thus a valuable tool enabling the design of the needed "electrical pathways" and the needed electric resistance properties, which allow multiple positive outcomes: (1) reduced power consumption for heating the material, (2) uniform microstructure and (3) improved material transparency.

Conclusions

A comprehensive, three-dimensional fully coupled thermo-electro-mechanical finite element framework has been developed for modeling the SPS process of the transparent alumina for three different tooling setups. The difficulties arise in the determination of the correct electrical resistance introduced by the different locations of the boron nitride layer.

Despite the deviations, the comparison of modeling and experimental results shows the capability of the model to provide good qualitative predictions of densification and grain growth behavior.

It is shown that the EE2 SPS tooling configuration (TM-SPS) renders the best SPS process outcomes. The benefits of the thermally managed SPS (EE2 configuration) are as follows: (1) improved transmittance of the central part of the specimen, (2) low power consumption, and (3) the uniform current flow preventing cracking of the specimen. All those combined advantages make the thermally managed SPS an attractive route for densifying a wide range of transparent ceramic materials with inherent energy saving.

Acknowledgements

The support of Minority Serving Institutions Science, Technology, Engineering and Mathematics Research and Development Consortium (MSRDC) (Award No: D01-W911-SR-14-2-0023) is gratefully appreciated. The support of US Army DEVCOM—Army Research Laboratory (Contract W911-NF-20-2-0226) is gratefully appreciated. The support of the National Science Foundation (Grants 2138421 and 2119832) is gratefully acknowledged. The support of the experimental part of the work by the US Department of Energy, Office of Basic Energy Sciences (Award No. SC0022244) is gratefully appreciated.

Author contributions

EAO, CWP and ET contributed to conceptualization; EAO, CWP, and ET contributed to methodology; ET contributed to software; ET and CWP contributed to validation; ET and CWP contributed to investigation; CWP and ET contributed to writing—original draft preparation; AEO, ET, CH and DM contributed to writing—review and editing; AEO contributed to supervision.

Funding

National Science Foundation, 2138421, Elisa Torresani, 2119832,Eugene A. Olevsky, Minority Serving Institutions Science, Technology, Engineering and Mathematics Research and Development Consortium, D01-W911-SR-14-2-0023, Eugene A. Olevsky, DEVCOM Army Research Laboratory,W911-NF-20-2-0226, Eugene A. Olevsky.

Data availability

The data that support the findings of this study are available from the corresponding author upon reasonable request.

Declarations

Conflict of interest The authors declare that they have no known competing financial interests or personal relationships that could have appeared to influence the work reported in this paper.

Ethical approval Not Applicable.

References

[1] Sun X, Wu H, Zhu G, Shan Y, Xu J, Li J, Olevsky EA (2020) Direct coarse powder aqueous slip casting and pressureless sintering of highly transparent AlON ceramics. Ceram Int 46(4):4850–4856

[2] Shan Y, Wei X, Sun X, Torresani E, Olevsky EA, Xu J (2019) Effect of heating rate on properties of transparent aluminum oxynitride sintered by spark plasma sintering. J Am Ceram Soc 102(2):662–673

[3] Park CW, In JH, Park JH, Shim KB, Ryu JH (2019) Up-and downconversion luminescence in Ho^{3+}, Yb^{3+}-Co-Doped Y_2O_3 transparent ceramics prepared by spark plasma sintering. Korean J Met Mater 57(9):609–616

[4] Patel PJ, Gilde GA, Dehmer PG, McCauley JW (2000) Transparent ceramics for armor and EM window applications. In Inorg Opt Mater 4102:1–14. https://doi.org/10.1117/12.405270

[5] Podowitz SR, Gaumé R, Feigelson RS (2010) Effect of europium concentration on densification of transparent Eu: Y_2O_3 scintillator ceramics using hot pressing. J Am Ceram Soc 93(1):82–88

[6] Wang J, Ma J, Zhang J, Liu P, Luo D, Yin D, Tang D, Kong LB (2017) Yb: Y_2O_3 transparent ceramics processed with hot isostatic pressing. Opt Mater 71:117–120

[7] Peuchert U, Okano Y, Menke Y, Reichel S, Ikesue A (2009) Transparent cubic-ZrO_2 ceramics for application as optical lenses. J Eur Ceram Soc 29(2):283–291

[8] Jin L, Zhou G, Shimai S, Zhang J, Wang S (2010) ZrO_2-doped Y_2O_3 transparent ceramics via slip casting and vacuum sintering. J Eur Ceram Soc 30(10):2139–2143

[9] Heidary DS, Lanagan M, Randall CA (2018) Contrasting energy efficiency in various ceramic sintering processes. J Eur Ceram Soc 38(4):1018–1029

[10] Agrafiotis C, Tsoutsos T (2001) Energy saving technologies in the European ceramic sector: a systematic review. Appl Therm Eng 21(12):1231–1249

[11] Olevsky EA, Dudina DV (2019) Field-assisted sintering: science and applications. Springer, New York

[12] Zhou Y, Hirao K, Yamauchi Y, Kanzaki S (2004) Densification and grain growth in pulse electric current sintering of alumina. J Eur Ceram Soc 24(12):3465–3470

[13] Groza JR, Zavaliangos A (2000) Sintering activation by external electrical field. Mater Sci Eng A 287(2):171–177

[14] Olevsky EA, Froyen L (2006) Constitutive modeling of spark-plasma sintering of conductive materials. Scr Mater 55(12):1175–1178

[15] Park CW, Lee JH, Kang SH, Park JH, Kim HM, Kang HS, Lee H, Lee JH, Shim KB (2017) Characteristics of Y_2O_3 transparent ceramics rapidly processed using spark plasma sintering. J Ceram Process Res 18(3):183–187

[16] Guillon O, Gonzalez-Julian J, Dargatz B, Kessel T, Schierning G, Räthel J, Herrmann M (2014) Field-assisted sintering technology spark plasma sintering mechanisms, materials, and technology developments. Adv Eng Mater 16(7):830–849

[17] Cheng L, Xie Z, Liu G (2013) Spark plasma sintering of TiC ceramic with tungsten carbide as a sintering additive. J Eur Ceram Soc 33(15–16):2971–2977

[18] Ratzker B, Sokol M, Kalabukhov S, Frage N (2018) High-pressure spark plasma sintering of silicon nitride with LiF additive. J Eur Ceram Soc 38(4):1271–1277

[19] Li X, Luo J, Zhou Y (2015) Spark plasma sintering behavior of AlON ceramics doped with different concentrations of Y_2O_3. J Eur Ceram Soc 35(7):2027–2032

[20] Castle E, Sheridan R, Grasso S, Walton A, Reece M (2016) Rapid sintering of anisotropic, nanograined Nd–Fe–B by flash-spark plasma sintering. J Magn Magn Mater 417:279–283

[21] Grasso S, Saunders T, Porwal H, Cedillos-Barraza O, Jayaseelan DD, Lee WE, Reece MJ (2014) Flash spark plasma sintering (FSPS) of pure ZrB_2. J Am Ceram Soc 97(8):2405–2408

[22] Vasylkiv O, Borodianska H, Sakka Y, Demirskyi D (2016) Flash spark plasma sintering of ultrafine yttria-stabilized zirconia ceramics. Scr Mater 121:32–36

[23] Grasso S, Saunders T, Porwal H, Milsom B, Tudball A, Reece M (2016) Flash spark plasma sintering (FSPS) of α and β SiC. J Am Ceram Soc 99(5):1534–1543

[24] Demirskyi D, Vasylkiv O (2017) Hot-spots generation, exaggerated grain growth and mechanical performance of silicon carbide bulks consolidated by flash spark plasma sintering. J Alloys Compd 691:466–473

[25] Anselmi-Tamburini U, Groza JR (2017) Critical assessment 28: electrical field/current application—a revolution in materials processing/sintering? Mater Sci Technol 33(16):1855–1862

[26] Giuntini D, Olevsky EA, Garcia-Cardona C, Maximenko AL, Yurlova MS, Haines CD, Martin DG, Kapoor D (2013) Localized overheating phenomena and optimization of spark-plasma sintering tooling design. Mater 6(7):2612–2632

[27] Manière C, Lee G, Olevsky EA (2017) All-materials-inclusive flash spark plasma sintering. Sci Rep 7(1):1–8

[28] Manière C, Lee G, McKittrick J, Olevsky EA (2019) Energy efficient spark plasma sintering: breaking the threshold of large dimension tooling energy consumption. J Am Ceram Soc 102(2):706–716

[29] Olevsky EA (1998) Theory of sintering: from discrete to continuum. Mater Sci Eng R Rep 23(2):41–100

[30] German RM (1996) Sintering theory and practice. John Wiley & Sons INC, New York, p 256

[31] Olevsky EA, Garcia-Cardona C, Bradbury WL, Haines CD, Martin DG, Kapoor D (2012) Fundamental aspects of spark plasma sintering: II. Finite element analysis of scalability. J Am Ceram Soc 95(8):2414–2422

[32] Wang Z, Zhang L, Yang H, Zhang J, Wang L, Zhang Q (2016) High optical quality Y_2O_3 transparent ceramics with fine grain size fabricated by low temperature air pre-sintering and post-HIP treatment. Ceram Int 42(3):4238–4245

[33] Zapata-Solvas E, Gómez-García D, Domínguez-Rodríguez A, Todd RI (2015) Ultra-fast and energy-efficient sintering of ceramics by electric current concentration. Sci Rep 5(1):1–7

[34] Wei Y, Gu S, Fang H, Luo W, Zhang X, Wang L, Jiang W (2020) Properties of MgO transparent ceramics prepared at low temperature using high sintering activity MgO powders. J Am Ceram Soc 103(9):5382–5391

[35] Kim BN, Hiraga K, Morita K, Yoshida H (2007) Spark plasma sintering of transparent alumina. Scri Mater 57(7):607–610

[36] Li Q, Zhang GP, Wang H, Lei LW (2011) Effect of pores on transmission properties of transparent ceramics. Optoelectron Adv Mater Rapid Commun 5:673–676

[37] Boniecki M, Librant Z, Wajler A, Wesołowski W, Węglarz H (2012) Fracture toughness, strength and creep of transparent ceramics at high temperature. Ceram Int 38(6):4517–4524

[38] Tani T, Miyamoto Y, Koizumi M, Shimada M (1986) Grain size dependences of Vickers microhardness and fracture toughness in Al_2O_3 and Y_2O_3 ceramics. Ceram Int 12(1):33–37